Journal of Materials Chemistry A

PAPER

View Article Online
View Journal | View Issue

Cite this: J. Mater. Chem. A, 2018, 6, 5971

General template-free strategy for fabricating mesoporous two-dimensional mixed oxide nanosheets *via* self-deconstruction/reconstruction of monodispersed metal glycerate nanospheres†

Yusuf Valentino Kaneti, *[a] Rahul R. Salunkhe,[ab] Ni Luh Wulan Septiani,[c] Christine Young,[a] Xuchuan Jiang,[d] Yan-Bing He,[e] Yong-Mook Kang,[f] Yoshiyuki Sugahara[gh] and Yusuke Yamauchi *[ij]

In this work, we propose a general template-free strategy for fabricating two-dimensional mesoporous mixed oxide nanosheets, such as metal cobaltites (MCo_2O_4, M = Ni, Zn) through the self-deconstruction/reconstruction of highly uniform Co-based metal glycerate nanospheres into 2D Co-based metal glycerate/hydroxide nanosheets, induced by the so-called "water treatment" process at room temperature followed by their calcination in air at 260 °C. The proposed 'self-deconstruction/reconstruction' strategy is highly advantageous as the resulting 2D metal cobaltite nanosheets possess very high surface areas (150–200 $m^2\ g^{-1}$) and mesoporous features with narrow pore size distribution. In addition, our proposed method also enables the crystallization temperature to achieve pure metal cobaltite phase from the precursor phase to be lowered by 50 °C. Using the 2D mesoporous $NiCo_2O_4$ nanosheets as a representative sample, we found that they exhibit 6–20 times higher specific capacitance and greatly enhanced capacitance retention compared to the $NiCo_2O_4$ nanospheres achieved through the direct calcination of the Ni–Co glycerate nanospheres. This highlights another advantage of the proposed strategy for enhancing the electrochemical performance of the mixed oxide products for supercapacitor applications. Furthermore, the asymmetric supercapacitor (ASC) assembled using the 2D $NiCo_2O_4$ nanosheets//graphene oxide (GO) exhibits a maximum energy density of 38.53 W h kg^{-1}, while also showing a high capacitance retention of 91% after 2000 cycles at 5 A g^{-1}. It is expected that the proposed general method may be extended to other transition metal elements for creating 2D mixed oxide nanosheets with enhanced surface areas and improved electrochemical performance.

Received 1st January 2018
Accepted 5th March 2018

DOI: 10.1039/c8ta00008e

rsc.li/materials-a

1. Introduction

Two-dimensional (2D) metal oxide nanomaterials have attracted significant research interests owing to their unique physical and chemical properties and ultra-high surface to volume ratio, which can provide many active sites for adsorption of ions or molecules or facilitate better transfer of ionic species.[1] As such, they have been utilized for a wide variety of applications, such as energy storage and conversion,[2,3] gas sensors,[4,5] catalysis,[6,7] and so on. To date, the synthesis of 2D transition metal oxide materials has been achieved using both gas- and liquid-phase methods. Gas-phase methods, such as chemical vapor

[a]International Center for Materials Nanoarchitectonics (WPI-MANA), National Institute for Materials Science (NIMS), 1-1 Namiki, Tsukuba, Ibaraki 305-0044, Japan. E-mail: KANETI.Valentino@nims.go.jp

[b]Department of Physics, Indian Institute of Technology Jammu, Paloura, Jammu, 181121, India

[c]Advanced Functional Materials (AFM) Laboratory, Engineering Physics, Bandung Institute of Technology, Bandung 40132, Indonesia

[d]Department of Chemical Engineering, Monash University, Clayton, VIC 3800, Australia

[e]Shenzhen Key Laboratory for Graphene-based Materials, Graduate School at Shenzhen, Tsinghua University, Shenzhen 518055, China

[f]Department of Energy and Materials Engineering, Dongguk University-Seoul, Seoul 04620, Republic of Korea

[g]Department of Applied Chemistry, School of Advanced Science and Engineering, Waseda University, 3-4-1, Okubo, Shinjuku-ku, Tokyo 169-8555, Japan

[h]Kagami Memorial Waseda Research Institute for Science and Technology, 2-8-26, Nishiwaseda, Shinjuku-ku, Tokyo 169-0054, Japan

[i]Department of Plant & Environmental New Resources, Kyung Hee University, 1732 Deogyeong-daero, Giheung-gu, Yongin-si, Gyeonggi-do 446-701, South Korea

[j]School of Chemical Engineering & Australian Institute for Bioengineering and Nanotechnology (AIBN), The University of Queensland, Brisbane, Queensland 4072, Australia. E-mail: y.yamauchi@uq.edu.au

† Electronic supplementary information (ESI) available. See DOI: 10.1039/c8ta00008e

deposition (CVD) can produce large-sized high-quality 2D oxide nanosheets on a substrate, however, they exhibit some disadvantages, including low yield, high energy consumption, and time consuming and complex procedures.[8] On the other hand, solution-based approaches, such as liquid exfoliation or wet-chemical processes are simpler to perform and scalable. However, they may lead to very small particles and have a higher probability of contamination from the synthetic process.[9] Other techniques, such as exfoliation are typically restricted to layered host materials, which limited their wider usage.

In recent years, several new wet-chemical methods have been developed for synthesizing 2D transition metal oxide (TMO) nanomaterials. For instance, Dou *et al.*[10] have demonstrated a generalized synthesis strategy for fabricating various ultrathin 2D TMO nanosheets (*e.g.* Co_3O_4, WO_3, TiO_2, *etc.*) by using the combination of both amphiphilic block copolymers (Pluronic 123) and short-chain alcohol to control the stacking and growth of the metal oxide nanoparticles along the chosen direction. However, such block copolymer-templated method requires careful control over the reaction process and crystal growth. Moreover, post-synthesis removal of the block copolymer is necessary to obtain well-crystallized 2D TMO nanosheets. Another recent strategy is by using salt microcrystals as templates to grow metal oxide precursor@salt composites through the mixing of inorganic salts with the metal oxide precursor solutions which could be converted to 2D TMO nanosheets (*e.g.*, MoO_3, MnO, and WO_3) following calcination at elevated temperatures.[9] While this method is easily scalable and provides a relatively large yield, the removal of the salts from the TMO nanosheets require careful filtration as incomplete clean-up of the remaining salts may impact the functional performance of the nanosheets.

Mixed oxide nanostructures have attracted tremendous interests owing to their enhanced electronic conductivity compared to pure metal oxides, as a result of the synergistic effect of various metallic species and the presence of multiple valencies of the contributing metals.[11] Among various mixed oxides, metal cobaltites (MCo_2O_4, M = Ni, Zn, Mn, *etc.*) have been widely investigated for energy storage applications owing to their layered structures, good electronic conductivity, and low manufacturing costs.[12,13] To date, 2D metal cobaltite nanosheets have been fabricated or grown on various conductive substrates through a variety of approaches, such as electrodeposition,[14] hydrothermal/solvothermal, microwave irradiation,[15] and co-precipitation.[16] However, the obtained nanosheets typically exhibit broad pore size distribution and low to moderate surface areas due to the change in their structural integrity from perfect nanosheets into nanoparticle-assembled nanosheets following calcination. Recently, 2D holey metal cobaltite nanosheets ($ZnCo_2O_4$ and $NiCo_2O_4$) have been successfully fabricated by growing the metal cobaltite precursors on graphene oxide (GO) *via* solution-phase reactions between transition metal ions and GO, which was partially reduced to reduced graphene oxide (rGO), followed by annealing to remove the rGO templates and promote crystallization of the nanosheets.[2] Although this method yields metal cobaltite nanosheets with strong mechanical properties inherited from the GO nanosheets, the method requires the initial synthesis of the GO template and subsequent removal of the GO template (to prevent carbon contamination), thereby complicating the synthesis process. Therefore, the development of a facile, general template-free strategy for synthesizing well-defined 2D mesoporous mixed oxide nanosheets with large surface areas (>150 $m^2 g^{-1}$) is highly desirable.

Herein, we report a general template-free strategy for obtaining 2D mesoporous mixed oxide nanosheets, such as metal cobaltites (MCo_2O_4, M = Ni, Zn) through the self-deconstruction/reconstruction of monodispersed cobalt (Co)-based metal glycerate nanospheres into 2D Co-based metal glycerate/hydroxide nanosheets followed by their calcination in air at a relatively low temperature of 260 °C. To induce the self-deconstruction/reconstruction, the as-synthesized Co-based metal glycerate nanospheres were subjected to a so-called "water treatment" process at room temperature for different duration. The proposed 'self-deconstruction/reconstruction' strategy is highly advantageous as the resulting 2D metal cobaltite nanosheets possess significantly higher surface areas (150–200 $m^2 g^{-1}$) than metal cobaltite nanospheres achieved by the direct annealing of the non-treated Co-based glycerate nanospheres (15–75 $m^2 g^{-1}$). Furthermore, these metal cobaltite nanosheets exhibit narrow pore size distribution in the mesoscale range, unlike the broad pore size distribution exhibited by the metal cobaltite nanospheres. In addition, the proposed method also enables the crystallization temperature to achieve pure metal cobaltite phase from the precursor phase to be lowered by 50 °C. Finally, as a representative sample, we have evaluated the electrochemical performance of the as-synthesized 2D mesoporous $NiCo_2O_4$ nanosheets for supercapacitor applications, in terms of specific capacitance, capacitance retention, stability, and also energy and power densities for asymmetric supercapacitor (ASC) device.

2. Experimental section

2.1. Chemicals

Cobalt(II) nitrate hexahydrate ($Co(NO_3)_2 \cdot 6H_2O$, 98%), nickel(II) nitrate hexahydrate ($Ni(NO_3)_2 \cdot 6H_2O$, 98%), zinc(II) nitrate hexahydrate ($Zn(NO_3)_2 \cdot 6H_2O$, 98%), glycerol ($C_3H_8O_3$, >99.5%), 2-propanol (C_3H_8O, >99.5%), and ethanol (C_2H_6O, 99.5%) were purchased from Wako Reagent Japan. All chemicals were used as received without further purification.

2.2. Synthesis of monodispersed cobalt (Co)-based metal glycerate nanospheres

In this work, monodispersed Co-based metal glycerate nanospheres (including Co, Ni–Co, Zn–Co) were firstly synthesized as seeds for the formation of 2D Co-based metal glycerate/hydroxide nanosheets. For example, in the synthesis of pure Co glycerate nanospheres, 0.1454 g (0.5 mmol) of $Co(NO_3)_2 \cdot 6H_2O$ was firstly dissolved in 40 mL of 2-propanol to form a pink-colored solution. Next, 8 mL of glycerol was added into this solution under magnetic stirring. Following this, the mixture solution was transferred into a Teflon-lined stainless steel autoclave and heated in an electric oven at 180 °C for 16 h.

Finally, the obtained precipitate was washed with absolute ethanol three times and then dried in an oven at 60 °C for 4 h. For the synthesis of Ni–Co and Zn–Co glycerate nanospheres, the synthesis procedures were almost similar, except that 0.25 mmol of $Ni(NO_3)_2 \cdot 6H_2O$ (0.0727 g) or 0.25 mmol of $Zn(NO_3)_2 \cdot 6H_2O$ (0.0744 g) was firstly mixed with the cobalt(II) nitrate solution prior to the addition of glycerol.

2.3. Conversion of Co-based metal glycerate nanospheres to 2D Co-based metal glycerate/hydroxide nanosheets *via* "water treatment" process

Co glycerate/hydroxide nanosheets. In a typical procedure, 20 mg of the as-synthesized Co-glycerate nanospheres was dispersed in 20 mL of distilled water and stirred for 6 h under mild stirring. After 6 h, the resulting product was washed twice with absolute ethanol, and dried in an oven at 60 °C for 4 h.

Ni–Co glycerate/hydroxide nanosheets. The conversion procedure for Ni–Co was very similar to that of Co-glycerate nanospheres, except that the Co-glycerate nanospheres were replaced with Ni–Co glycerate nanospheres and the dispersion time in water was extended to 24 h.

Zn–Co glycerate/hydroxide nanosheets. In a typical synthesis, 20 mg of the Zn–Co glycerate nanospheres was dispersed in a water (10 mL)/ethanol (10 mL) mixture and reacted for 4 h under mild stirring. After 4 h, the resulting product was washed twice with absolute ethanol, and dried in an oven at 60 °C for 4 h.

2.4. Conversion to porous 2D metal cobaltite nanosheets

The porous 2D Co_3O_4, $NiCo_2O_4$ and $ZnCo_2O_4$ nanosheets were obtained by calcination of the Co, Ni–Co and Zn–Co glycerate/hydroxide nanosheets, respectively, in air at 260 °C, under a slow heating rate of 1 °C min^{-1}.

2.5. Characterization

X-ray diffraction (XRD) patterns of the samples were obtained using a Rigaku RINT 2500X diffractometer with a monochromated Cu-Kα radiation ($\lambda = 1.5418$ Å). The morphological observations of the samples were conducted using field-emission scanning electron microscope (FESEM, Hitachi SU-8000) operated at an accelerating voltage of 5 kV and transmission electron microscope (TEM, JEM-2100F) operated at an accelerating voltage of 200 kV. The thermogravimetric analysis (TGA) of the samples was performed using a Hitachi HT-Seiko Instrument Exter 6300 TG/DTA under air atmosphere with a constant heating rate of 10 °C min^{-1} from room temperature to 600 °C. X-ray photoelectron spectroscopy (XPS) measurements were carried out with a PHI Quantera SXM (ULVAC-PHI) using Al-Kα radiation as the excitation source to determine the composition and electronic state of the as-prepared samples. All XPS spectra were calibrated to the C 1s peak at 285.0 eV. Nitrogen (N_2) adsorption–desorption measurements were performed using a Belsorp-mini II Sorption System at 77 K. The specific surface areas were calculated using the multipoint Brunauer–Emmett–Teller (BET) method at a relative pressure (P/P_0) range of 0.05 to 0.30 and the total pore volumes were calculated by the Barrett–Joyner–Halenda (BJH) method. Prior to the BET measurements, the samples were degassed under vacuum at 150 °C for overnight.

2.6. Electrochemical measurements

The electrochemical measurements were carried out with an electrochemical workstation (CHI 660E, CH Instruments, USA) using standard three-electrode and two-electrode system measurements. For the three-electrode system, Ag/AgCl was used as the reference electrode and a platinum wire was used as a counter electrode and all the measurements were carried out in an aqueous 3.0 M KOH electrolyte. The working electrodes were prepared by mixing the active electrode material (80%) with poly(vinylidene difluoride) (PVDF) (20%) in *N*-methylpyrrolidinone (NMP). The resultant slurry was then coated onto graphite substrates and dried at 60 °C for 12 h. Each electrode contained 1 mg cm^{-2} of the active material. The specific capacitance of each electrode was calculated using cyclic voltammetry (CV) with the following equation:

$$C = \frac{1}{ms\left(V_f - V_i\right)} \int_{V_i}^{V_f} I(V)\mathrm{d}V \quad (1)$$

where C is the specific capacitance, s is potential scan rate, V is the potential window, the integration of $I(V)\mathrm{d}V$ is the discharging part of the cyclic voltammograms, and m is the mass of the active material. The two electrode-system consists of two electrodes of similar charge capacity separated by an electrolyte at a distance of ~0.5 cm. The specific capacitance was calculated by utilizing the following equation:

$$C = \frac{I \times \int V\mathrm{d}t}{M \times \Delta V^2} \quad (2)$$

where C is the gravimetric capacitance, V is a potential window, I is the current, t is the discharge time, and M is the total mass of active materials of both electrodes.

The electrochemical properties of the assembled asymmetric supercapacitor (ASC) cell were investigated by using CV and galvanostatic charge–discharge (CD) measurements. For the CD measurements of the two-electrode ASC cell, a positive electrode consisting of 2D $NiCo_2O_4$ nanosheets and a negative electrode consisting of graphene oxide (GO) with a similar charge capacity were employed. To achieve a stable ASC cell operated over a wide potential window, it is important to achieve a mass balance between the positive and negative electrodes, according to the equation:

$$\frac{m_+}{m_-} = \frac{C_- V_-}{C_+ V_+} \quad (3)$$

where C_+ and C_- are the specific capacitances, V_+ and V_- are the potential windows, and m_+ and m_- are the mass of the positive and negative electrode materials, respectively, which were obtained in a three-electrode system. In the case of symmetric (or linear) galvanostatic discharge curve (GDC) behavior, the charge/voltage ratio remains constant over the entire voltage window, and the energy density E can be calculated by applying the following equation:[17]

$$E = \frac{CV^2}{2} \quad (4)$$

However, our GDC is non-symmetric and hence, the Faradaic reaction charge/voltage ratio does not remain constant, but rather varies with time.[17–19] As such, the energy density (E) and power density (P) of the assembled ASC were calculated using the equations:[17]

$$E = i\int V\mathrm{d}t \quad (5)$$

$$P = \frac{3600 \times E}{t} \quad (6)$$

where i is the current density, $\int V\mathrm{d}t$ is the galvanostatic discharge current area and t is the discharge time.

3. Results and discussion

3.1 Morphology and composition

Scheme 1 illustrates the proposed general strategy for obtaining 2D mesoporous mixed oxide nanosheets, such as metal cobaltites [MCo_2O_4 (M = Ni, Zn)] as examples. First, monodispersed Co-based metal glycerate nanospheres are synthesized through the solvothermal reactions of metal nitrates and glycerol in 2-propanol at 180 °C and used as self-templates for the subsequent conversion steps. Next, these metal glycerate nanospheres are subjected to "water treatment" at room temperature, in which they are dispersed in water for different duration to induce surface deconstruction of the nanospheres due to the attack by the hydroxide (OH^-) ions present in the water (step i in Scheme 1a). As the reaction progresses, sheet-like sub-units gradually grow on the surface of these nanospheres, eventually reconstructing their surface, leading to the formation of hierarchical 3D flower-like nanosheets (step ii in Scheme 1a). Finally, with prolonged treatment time, the nanospheres which had formed the base of these hierarchical 3D flower-like structures collapse, thus allowing the nanosheets which initially grew only on the surface of the nanospheres to grow laterally to form 2D Co-based metal glycerate/hydroxide nanosheets (step iii in Scheme 1a). Following calcination in air at a relatively low temperature of 260 °C, these 2D Co-based metal glycerate/hydroxide nanosheets are successfully converted to 2D mesoporous metal cobaltite nanosheets (step iv in

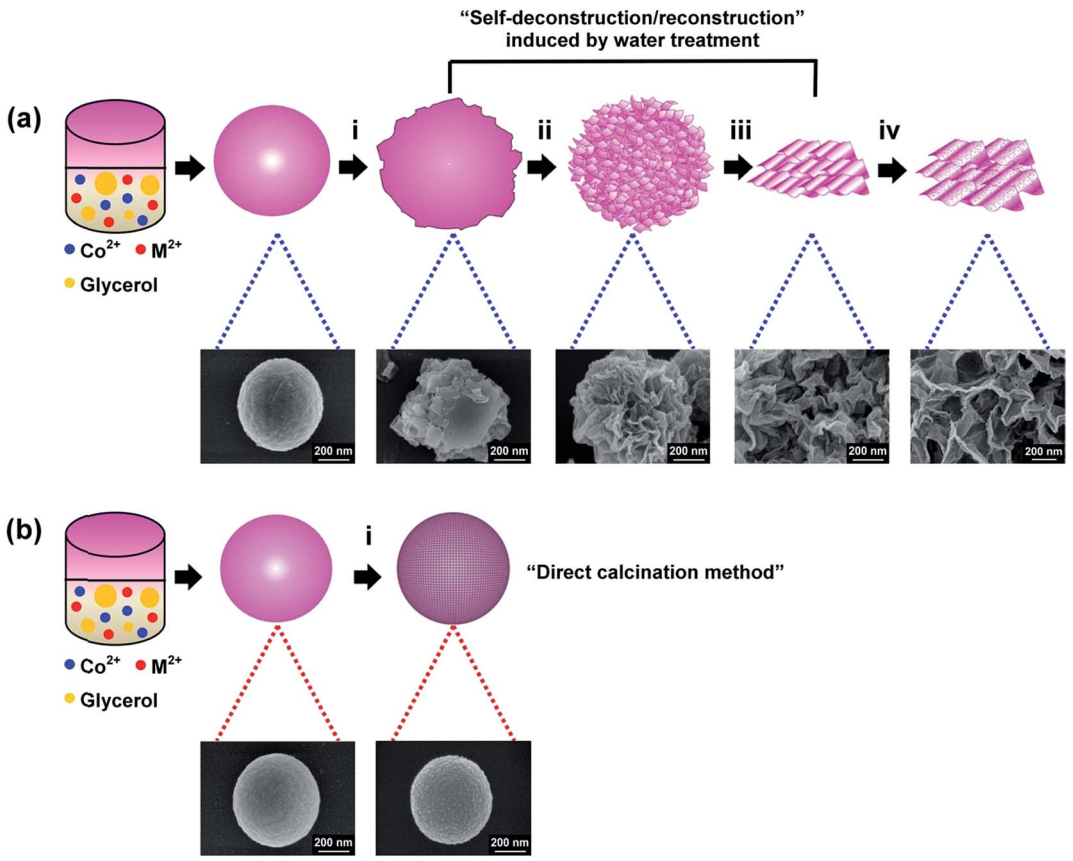

Scheme 1 (a) Schematic illustration showing the proposed general template-free strategy for obtaining mesoporous 2D mixed oxide nanosheets, such as metal cobaltites (MCo_2O_4, M = Ni, Zn) as examples: (i) surface deconstruction of the Co-based metal (M-Co) glycerate nanospheres induced by the "water treatment" process; (ii) surface reconstruction of the M-Co glycerate nanospheres to form hierarchical 3D flower-like nanosheets; (iii) lateral growth of the sheet-like structures assembling the hierarchical 3D structures to form 2D M-Co glycerate/hydroxide nanosheets; (iv) conversion into mesoporous 2D MCo_2O_4 nanosheets *via* calcination in air at 260 °C. (b) Schematic illustration of the method for obtaining porous MCo_2O_4 (M = Ni, Zn) nanospheres by direct calcination of the M-Co glycerate nanospheres in air at 350 °C (step i).

Scheme 1a). The presented work is different from previous reports,[20,21] in which hierarchical 3D hollow spheres were obtained from the consumption metal glycerate nanospheres during solvothermal reactions in mixed alcohol-based solvents at high temperatures and no 2D mesoporous nanosheets were reported in these studies. In our work, 2D nanosheets were obtained from a simple prolonged reaction of metal glycerate nanospheres in water at room temperature which results in gradual breakdown of the organic groups present in the glycerate nanospheres and their subsequent replacement with hydroxyl nanosheets.

The phase composition and crystal structures of the Co-based metal glycerate nanospheres obtained from the solvothermal reactions at 180 °C were analyzed by XRD. As shown in Fig. S1a–c,† these particles are mostly amorphous, however a pronounced broad diffraction peak is observed at ~12° in all three samples, which is the characteristic peak of metal glycerates.[22,23] Correspondingly, these three products can be assigned as Co, Ni–Co, and Zn–Co glycerate, respectively. The SEM images shown in Fig. 1a–f reveal that the as-obtained Co, Ni–Co, and ZnCo glycerate nanospheres are highly uniform in shape with the average diameters being 760, 663, and 779 nm, respectively. The time-dependent morphological evolution of the Co-based metal glycerate nanospheres into 2D nanosheets as a result of the "water treatment" process was monitored by SEM, as presented in Fig. 2. The formation of some very thin sheet-like sub-units is readily observed on the surface of the Co and Ni–Co glycerate nanospheres after 2 h and 4 h of "water treatment", respectively (Fig. 2b, f). When the reaction time is extended for a further 2 h, the sheet-like sub-units grow on the surface of the Co and Ni–Co glycerate nanospheres to form 3D hierarchical flower-like nanosheets (Fig. 2c, g). Finally, at the optimized reaction times of 6 h (for Co glycerate) and 24 h (for Ni–Co glycerate), ultrathin 2D nanosheets are successfully formed from the lateral growth of the nanosheets which assembled the hierarchical 3D flower-like structures (Fig. 2d, h). In the case of Zn–Co glycerate, the use of a water/ethanol mixture is necessary to slow down the rate of release of OH^- ions, which would have otherwise lead to the formation of aggregated particles rather than uniform 2D nanosheets. Following the "water treatment" process, the XRD patterns of the Co, Ni–Co, and Zn–Co glycerate nanospheres display two new peaks at ~34° and ~60°, indexed to hydroxide phases (Co hydroxide, Ni–Co double hydroxides, and Zn–Co double hydroxides, respectively), in addition to the broad glycerate peak at ~12°.[24,25] These results imply that the composition of the water-treated products can be assigned as Co, Ni–Co, and Zn–Co glycerate/hydroxide mixtures, respectively.

The self-deconstruction/reconstruction of the Co-based metal glycerate nanospheres (Fig. 3a, e and i) with increasing "water treatment" time is shown more clearly in the SEM images shown in Fig. 3. Evidently, the three samples (Co, Ni–Co and Zn–Co) follow a similar mechanism, in which the surface of the nanospheres undergoes self-deconstruction in the initial stage of the reaction due to the attack by the OH^- ions present in the water (Fig. 3b, f, j) and slowly being reconstructed by the nanosheets formed on the surface of the nanospheres (Fig. 3c, g, k). The growth of such hierarchical flower-like structures may be attributed to the formation of metal or mixed-metal hydroxide phases during the early stage of the water treatment, which are known for their layered structures and their strong tendency to assume sheet-like morphology. After prolonged "water treatment", the base nanospheres collapse and the nanosheets whose growth were initially bound to the surface of the nanospheres become free to grow laterally, thereby leading to the formation of 2D nanosheets (Fig. 3d, h and l).

FTIR spectroscopy was conducted to analyze the changes in organic constituents of the Co, Ni–Co, and Zn–Co glycerate nanospheres with increasing "water treatment" time. For the non-treated Co, Ni–Co, and Zn–Co glycerate nanospheres (Fig. 4a, d and g (0 h)), the broad IR absorption band between 3200–3400 cm^{-1} can be assigned to hydrogen-bound hydroxyl groups, whereas the absorption bands between 2850–2950 cm^{-1} can be indexed to the C–H stretching vibrations.[26] The IR band located between ~1640–1650 cm^{-1} is attributed to the C=O stretching vibration while the band located at ~1585 cm^{-1} is assigned to the C=C stretching vibration. Moreover, the absorption bands in the range of 1300–1400 cm^{-1}, 1000–1200 cm^{-1}, and 850–1000 cm^{-1} can be attributed to C–H bending vibration, C–O stretching vibration, and C–C stretching vibration, respectively. As shown in Fig. 4a, d, g, the increase in "water treatment" time is observed to shift the broad O–H peak closer toward 3600 cm^{-1} for all three samples (Co, Ni–Co, and Zn–Co), indicating the gradual transformation toward structurally isolated hydroxyls (*i.e.* metal hydroxides). Furthermore, weakening of the C–H bending and C–C stretching vibrations is

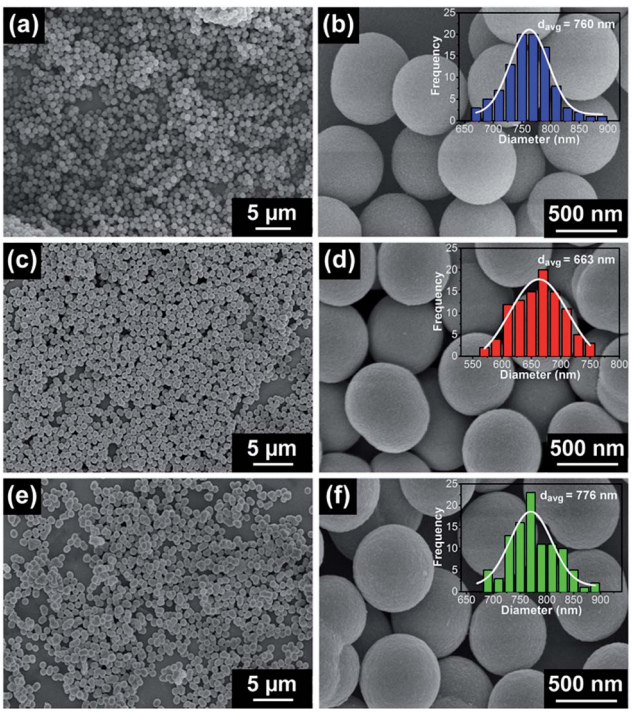

Fig. 1 Low and high magnification SEM images of (a, b) pure Co, (c, d) Ni–Co, and (e, f) Zn–Co glycerate nanospheres (insets showing the corresponding size distribution histograms).

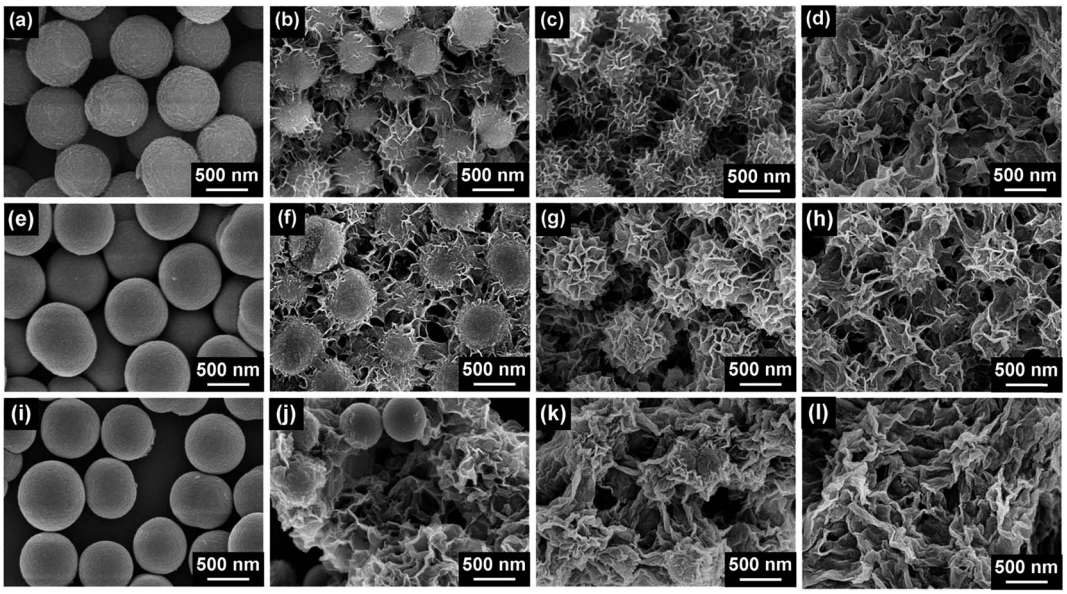

Fig. 2 Time-dependent SEM images of the Co glycerate nanospheres after subjected to "water treatment" process for (a) 0 h, (b) 2 h, (c) 4 h, and (d) 6 h. Time-dependent SEM images of the Ni–Co glycerate nanospheres after subjected to "water treatment" process for (e) 0 h, (f) 4 h, (g) 6 h, and (h) 24 h. Time-dependent SEM images of the Zn–Co glycerate nanospheres after treatment in a water/ethanol (v/v = 1 : 1) mixture for (i) 0 h, (j) 2 h, (k) 4 h, and (l) 6 h.

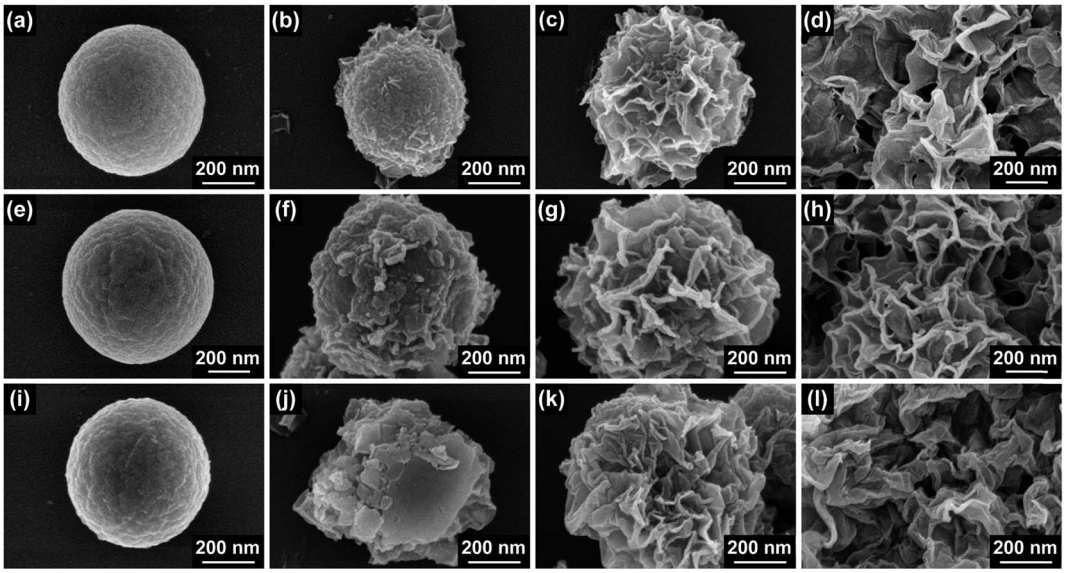

Fig. 3 SEM images showing the stages of conversion from smooth nanospheres to 2D nanosheets: (a, e, i) original glycerate sphere, (b, f, j) surface-deconstructed sphere, (c, g, k) surface reconstruction of the sphere by nanosheets, and (d, h, l) lateral growth of the nanosheets to form 2D structures for Co, Ni–Co and Zn–Co samples, respectively.

observed with increasing treatment time (Fig. 4b, e, h), indicating the partial removal of these organic groups. In addition, the gradual disappearance of the C=O stretching vibration and weakening of the C=C stretching vibration are also observed in all three samples (Fig. 4c, f, i). These IR results suggest that compositionally, the 2D nanosheets obtained from the "water treatment" of the Co-based metal glycerate nanospheres consist of a mixture of glycerate and hydroxide and this confirms the XRD results.

TGA measurements were performed on both the Co-based metal glycerate nanospheres and Co-based metal glycerate/hydroxide nanosheets to assess the effect of the "water treatment" process on the crystallization temperature required to obtain pure metal cobaltite phase. The TGA curves of the non-treated Co, Ni–Co, and Zn–Co glycerate nanospheres (Fig. 5a–c) show two main weight loss steps, with the first weight loss occurring at around 150 °C due to the removal of adsorbed water molecules, and the second one occurring at around

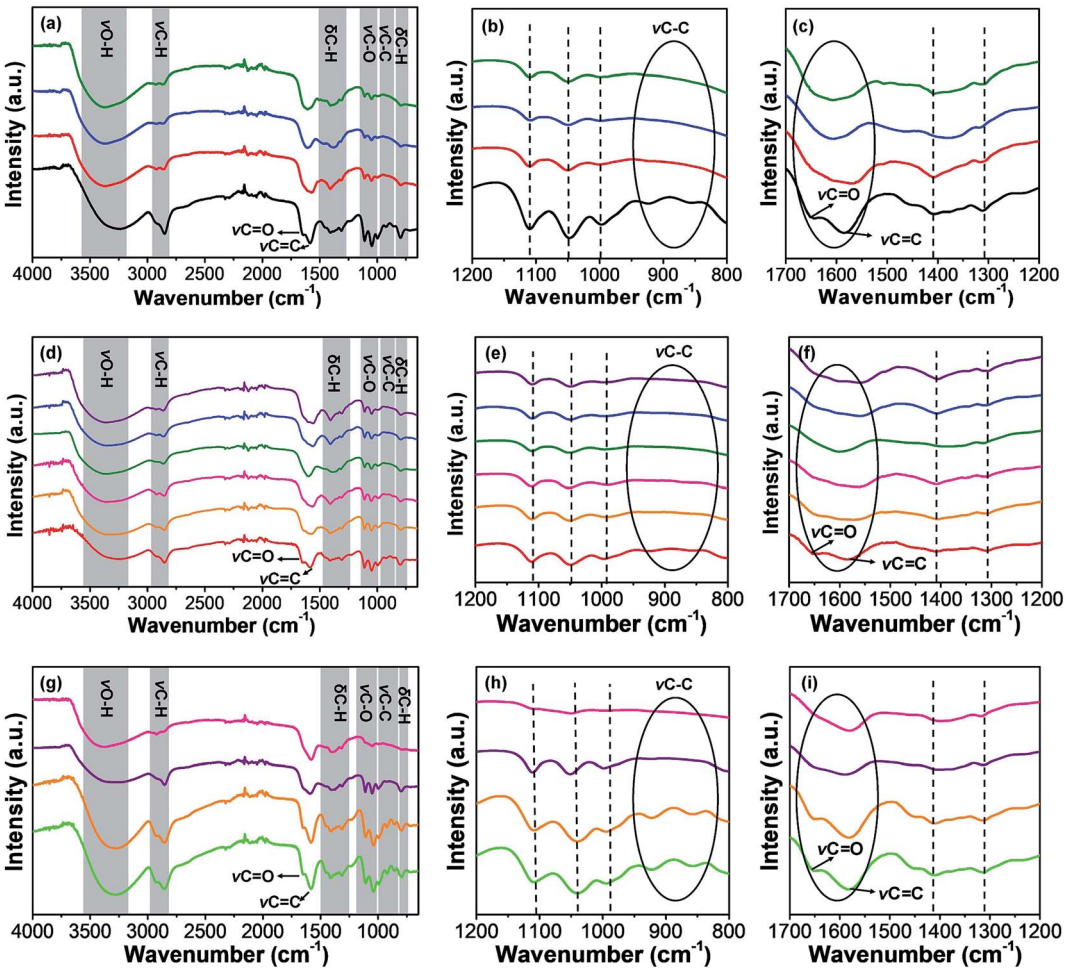

Fig. 4 (a) Overall FTIR spectra, (b) enlarged FTIR spectra from 800–1200 cm^{-1}, and (c) enlarged FTIR spectra from 1200–1700 cm^{-1} of Co glycerate nanospheres with increasing "water treatment" time (from bottom to top: 0 h, 2 h, 4 h, and 6 h). (d) Overall FTIR spectra, (e) enlarged FTIR spectra from 800–1200 cm^{-1}, and (f) enlarged FTIR spectra from 1200–1700 cm^{-1} of Ni–Co glycerate nanospheres with increasing "water treatment" time (from bottom to top: 0 h, 2 h, 4 h, 6 h, 16 h, and 24 h). (g) Overall FTIR spectra, (h) enlarged FTIR spectra from 800–1200 cm^{-1}, and (i) enlarged FTIR spectra from 1200–1700 cm^{-1} of Zn–Co glycerate nanospheres with increasing "water treatment" time (from bottom to top: 0 h, 2 h, 4 h, and 6 h).

300 °C due to the removal of the organic constituents and subsequent transformation to metal oxides. Similarly, the Co, Ni–Co, and Zn–Co glycerate/hydroxide nanosheets also display two weight loss steps, however, the amount of weight loss due to adsorbed water molecules is two-times higher than those observed for Co, Ni–Co, and Zn–Co glycerate spheres (Fig. 5d–f). Correspondingly, the weight loss percentage due to the decomposition of organic constituents is decreased by half for Co, Ni–Co, and Zn–Co glycerate/hydroxide nanosheets. These trends reveal the obvious increase in the hydroxide content of the precursor nanosheets following the "water treatment" process, thereby confirming their mixed composition (*i.e.* glycerate/hydroxide mixtures). Furthermore, the TGA curves in Fig. 5 reveal that the crystallization temperature for obtaining pure metal cobaltite phase is decreased by ~50 °C to 260 °C for all three samples following the conversion of the nanospheres to 2D nanosheets and this temperature is among the lowest conversion temperature reported in literatures (see Table S1†). The above results clearly indicate the benefit of the proposed 'self-deconstruction/reconstruction' strategy for decreasing the crystallization temperature necessary for obtaining pure metal cobaltite products. Accordingly, the calcination of the 2D Co, Ni–Co, and Zn–Co glycerate/hydroxide nanosheets at 260 °C yielded pure Co_3O_4, $NiCo_2O_4$ and $ZnCo_2O_4$, respectively, as confirmed by the XRD patterns shown in Fig. S3.† This is further supported by the EDS analysis of the calcined 2D nanosheets provided in Fig. S4.†

Fig. 6a–c show the typical SEM images of the 2D Co_3O_4, $NiCo_2O_4$ and $ZnCo_2O_4$ nanosheets obtained by calcination of the 2D Co, Ni–Co, and Zn–Co glycerate/hydroxide nanosheets, respectively. The original nanosheet structure is well-retained without significant destruction into small nanocrystals and no significant aggregation among the nanosheets is observed. From the three metal cobaltite nanosheets, the $NiCo_2O_4$ nanosheets show the smallest thicknesses of 5–7 nm, whereas the thicknesses of the 2D Co_3O_4 and $ZnCo_2O_4$ nanosheets vary from 6–15 nm and 9–18 nm, respectively. The porous nature of these nanosheets can be observed from the TEM images in Fig. S5a–

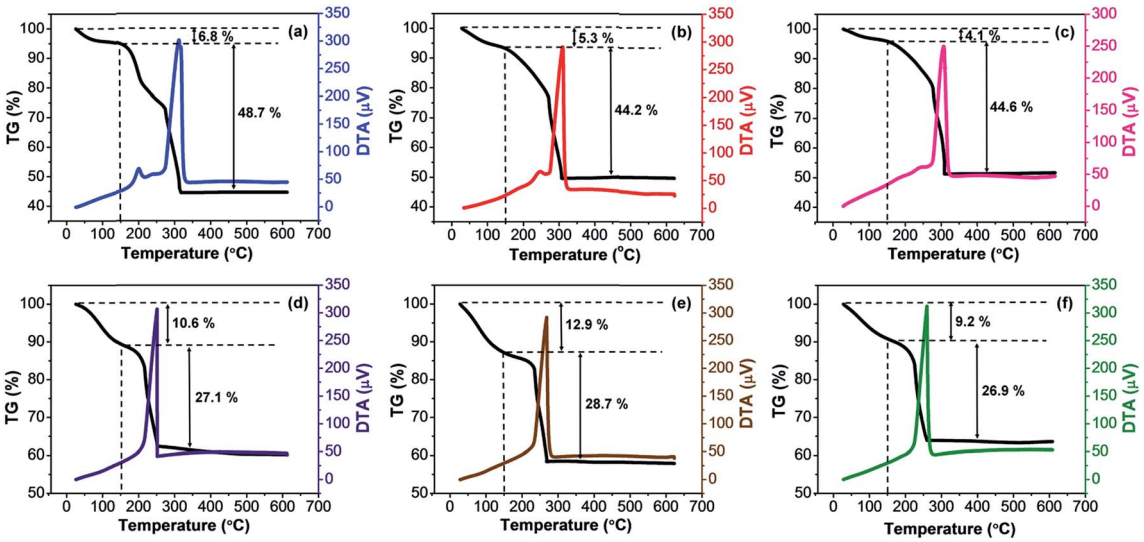

Fig. 5 (a–c) TG-DTA curves of Co, Ni–Co, and Zn–Co glycerate nanospheres and (d–f) TG-DTA curves of Co, Ni–Co, and Zn–Co glycerate/hydroxide nanosheets obtained using the proposed 'self-deconstruction/reconstruction' strategy.

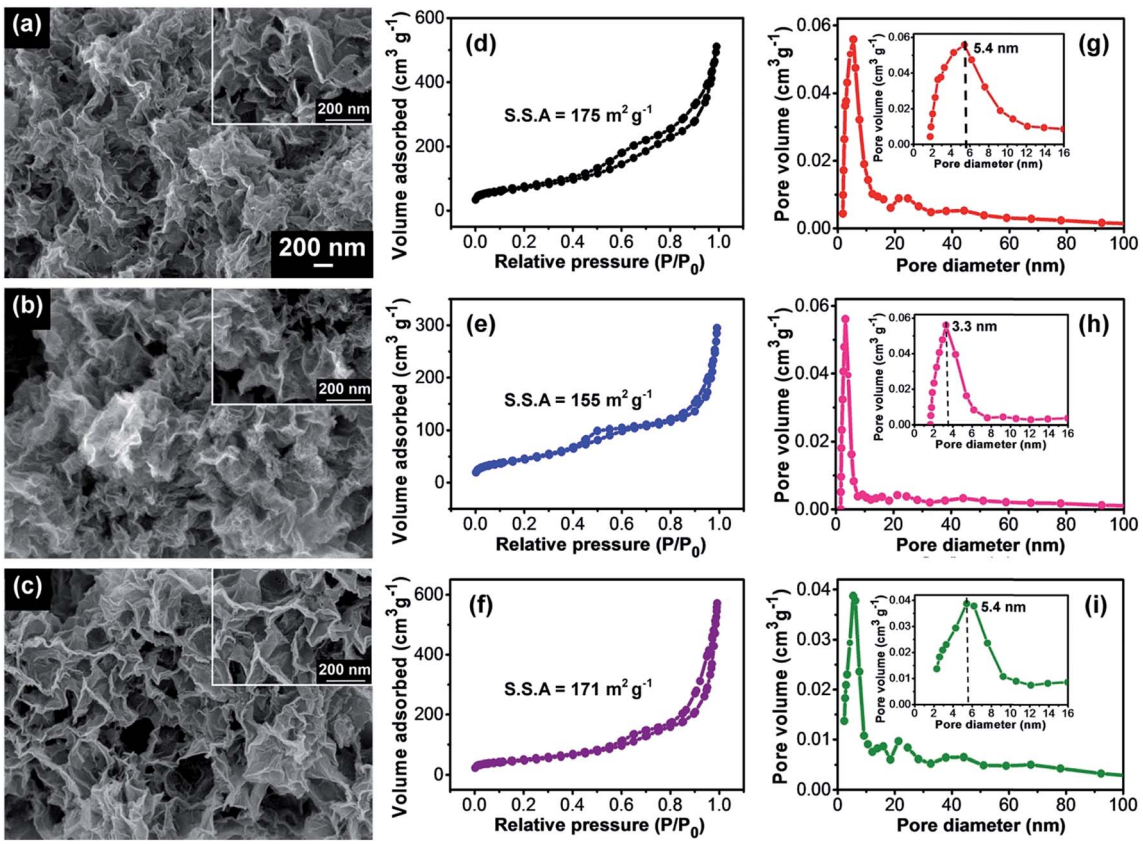

Fig. 6 SEM, N_2 adsorption–desorption isotherms and BJH pore size distribution curves of mesoporous 2D Co_3O_4 (a, d and g), $NiCo_2O_4$ (b, e and h), and $ZnCo_2O_4$ (c, f and i) nanosheets obtained by calcination of the 2D Co, Ni–Co and Zn–Co glycerate/hydroxide nanosheets, achieved using the proposed 'self-deconstruction/reconstruction' strategy, respectively, in air at 260 °C.

c,† which originated from the release of H_2O and CO_2 during the heat treatment at 260 °C.[25] The HRTEM images of the Co_3O_4, $NiCo_2O_4$ and $ZnCo_2O_4$ nanosheets show well-defined lattice fringes corresponding to the (111), (220), and (311) planes of Co_3O_4 (Fig. S5d†), (400) and (311) planes of $NiCo_2O_4$ (Fig. S5e†), and (311) and (220) planes of $ZnCo_2O_4$ (Fig. S5f†),

respectively. N_2 adsorption–desorption isotherms of the 2D Co_3O_4, $NiCo_2O_4$ and $ZnCo_2O_4$ nanosheets synthesized using the proposed 'self-deconstruction/reconstruction' strategy reveal their very high surface areas of 175, 155, and 171 $m^2\ g^{-1}$ (Fig. 6d–f), respectively. These values are approximately 2.5–10 times higher than those of the corresponding metal cobaltite nanospheres (18.7, 16.1, and 71.6 $m^2\ g^{-1}$, respectively) (Fig. S6a–c†). In fact, these surface area values are among the highest reported values for 2D metal cobaltite nanostructures, as evident in Table S1.† Moreover, the BJH pore distribution curves of the as-obtained 2D metal cobaltite nanosheets reveal their mesoporous features with narrow pore size distribution in the range of 2–10 nm (Fig. 6g–i). In contrast, the Co_3O_4, $NiCo_2O_4$, and $ZnCo_2O_4$ nanospheres all show broad pore size distribution with pore sizes ranging from 2–40 nm (Fig. S6d–f†). These results therefore highlight the advantages of our proposed strategy for increasing the specific surface area and narrowing the pore size distribution of the metal oxide products (see Table 1).

XPS analysis was conducted to analyze the surface chemical states and composition of the 2D mesoporous metal cobaltite nanosheets obtained using the proposed 'self-deconstruction/reconstruction' method. The high-resolution spectrum of Co 2p of the $NiCo_2O_4$ nanosheets shows two spin–orbit doublets (Co^{2+} and Co^{3+}) and two shake-up satellites (Fig. 7a). The peaks at 780.1 eV and 795.2 eV are attributed to Co^{3+} and the peaks at 781.8 eV and 797.1 eV are indexed to Co^{2+}.[27] The O 1s high resolution spectrum of the $NiCo_2O_4$ nanosheets (Fig. 7b) exhibits three distinct oxygen species labeled as O_I, O_{II}, and O_{III}. The O_I peak at a binding energy of 529.6 eV is typical of metal–oxygen bonds, whereas the O_{II} and O_{III} peaks at binding energies of 531.7 eV and 532.7 eV correspond to the high number of defect sites with low oxygen coordination in the material with small particle size and physi- or chemisorbed water molecules, respectively. The Ni 2p spectrum of the $NiCo_2O_4$ nanosheets can also be fitted into two spin–orbit doublets (Ni^{2+} and Ni^{3+}) and two shake-up satellites (Fig. 7c). The peaks at 854.2 eV and 871.8 eV are attributed to Ni^{2+} and the peaks at 855.8 eV and 873.3 eV can be assigned to Ni^{3+}, indicating the mixed valence nature of the Ni in $NiCo_2O_4$ nanosheets.[28,29] Similar to $NiCo_2O_4$, the Co 2p spectra of the $ZnCo_2O_4$ nanosheets also exhibit two spin–orbit doublets and two-shake up satellites, as shown in Fig. 7d. The two peaks corresponding to Co^{3+} are located at binding energies of 780.2 eV and 795.2 eV, respectively, whereas the peaks attributed to Co^{2+} are observed at binding energies of 781.4 eV and 796.8 eV, respectively. The O 1s high-resolution XPS spectrum of the 2D $ZnCo_2O_4$ nanosheets can be deconvoluted into three distinct peaks, corresponding to the same oxygen species present in the $NiCo_2O_4$ nanosheets (Fig. 7e). Furthermore, the Zn 2p spectrum displays two major peaks at binding energies of 1021.2 eV and 1044.5 eV, which can be assigned to Zn $2p_{3/2}$ and Zn $2p_{1/2}$, respectively, indicating the Zn^{2+} oxidation state of $ZnCo_2O_4$ (Fig. 7f).[29,30] In comparison, for the Co_3O_4 nanosheets, the Co^{3+} peaks are positioned at binding energies of 780.1 eV and 795.2 eV, respectively and the Co^{2+} peaks are observed at binding energies of 781.8 eV and 797.2 eV, respectively (Fig. 7g), with the O 1s spectrum showing the same three distinct oxygen species as their mixed oxide counterparts (Fig. 7h).[31] The above XPS results therefore indicate the mixed valence of Co in all of the synthesized metal cobaltite nanosheets. The binding energy values of Co 2p, Ni 2p, and Zn 2p peaks of the as-synthesized metal cobaltite nanosheets are in good agreement with previous literatures, as summarized in Table S2.†

3.2 Electrochemical performance

Inspired by their large surface area and mesoporous features, we have evaluated the electrochemical performance of the as-obtained 2D metal cobaltite nanosheets for supercapacitor applications. Fig. 8a compares the cyclic voltammogram (CV) curve of the 2D $NiCo_2O_4$ nanosheets with that of the $NiCo_2O_4$ nanospheres at a scan rate of 20 mV s^{-1}, revealing their higher current density and CV curve area, and therefore higher electrochemical activity compared to the nanospheres.[32] Similarly, both Co_3O_4 and $ZnCo_2O_4$ nanosheets also display higher current densities compared to their corresponding nanospheres (Fig. S7a, b†). This may be correlated to the significantly larger surface area and pore volume of the metal cobaltite nanosheets (~10 times higher) which enable a higher storage of electrolyte ions. Among the three metal cobaltite nanosheets, the $NiCo_2O_4$ nanosheets show the highest electrochemical performance and therefore, for further studies we have chosen this particular sample to show the benefit of our proposed strategy for enhancing the electrochemical performance of the metal oxide products.

Fig. 8b shows the typical CV curves of the $NiCo_2O_4$ nanosheets at various scan rates from 5 to 100 mV s^{-1}. The shape of the CV curves reveals the typical pseudocapacitive characteristics. A pair of well-defined redox peaks (cathodic and anodic peaks at ~0.28 V and 0.37 V) is observed at low scan rates (*e.g.* 5 mV s^{-1}), which can be attributed to the faradaic redox

Table 1 Comparison of the properties of 2D mesoporous metal cobaltite nanosheets obtained using the proposed 'self-deconstruction/reconstruction' strategy with the metal cobaltite nanospheres achieved by the direct calcination of the Co-based metal glycerate nanospheres

Properties	Co_3O_4 nanospheres	2D Co_3O_4 nanosheets	$NiCo_2O_4$ nanospheres	2D $NiCo_2O_4$ nanosheets	$ZnCo_2O_4$ nanospheres	2D $ZnCo_2O_4$ nanosheets
Crystallization temperature (°C)	320	260	310	260	310	260
Specific surface area ($m^2\ g^{-1}$)	18.7	175	16.3	155	71.6	171
Pore volume ($cm^3\ g^{-1}$)	0.127	0.785	0.057	0.452	0.207	0.867

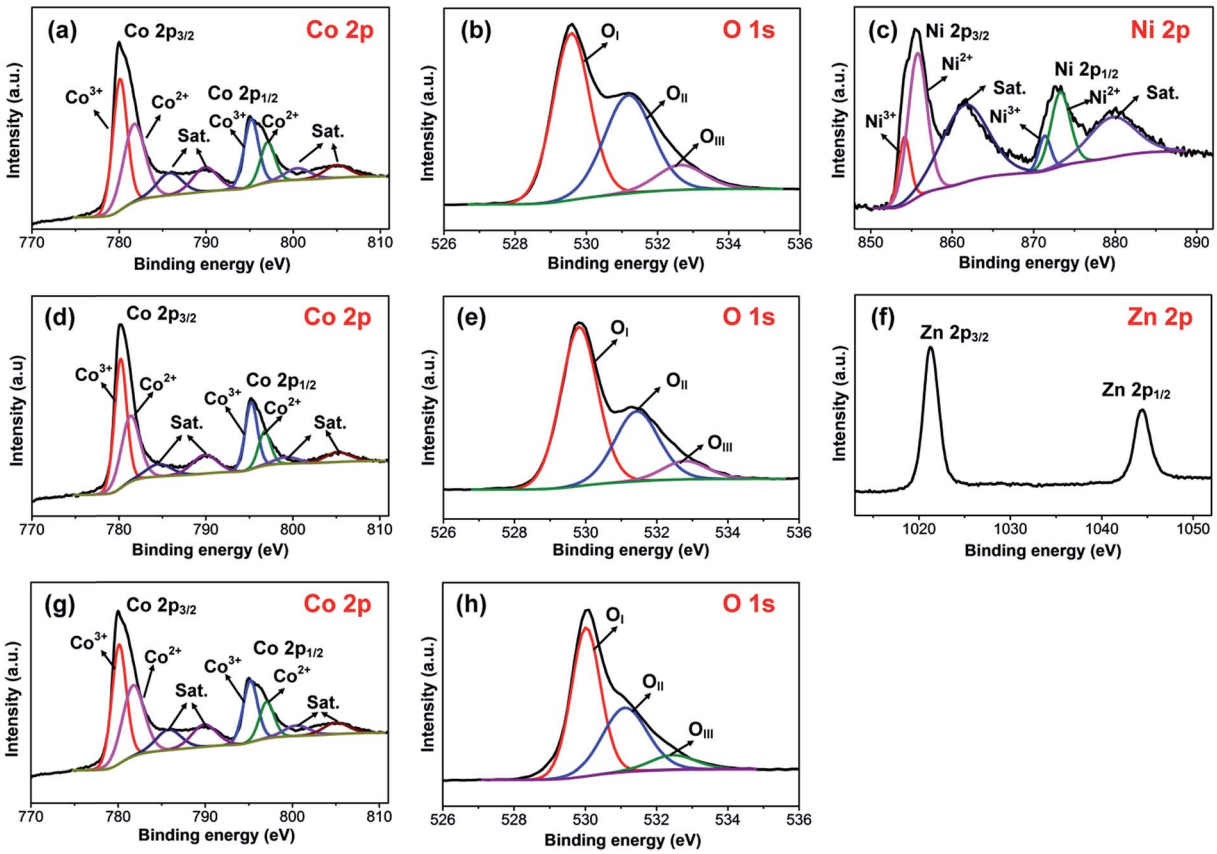

Fig. 7 High resolution XPS spectra of (a) Co 2p, (b) O 1s, and (c) Ni 2p for $NiCo_2O_4$ nanosheets. High resolution XPS spectra of (d) Co 2p, (e) O 1s, and (f) Zn 2p for $ZnCo_2O_4$ nanosheets. High resolution XPS spectra of (g) Co 2p and (h) O 1s for Co_3O_4 nanosheets.

reactions of $NiCo_2O_4$ in the KOH electrolyte based on the following equations:[13,33,34]

$$NiCo_2O_4 + OH^- + H_2O \rightleftharpoons NiOOH + 2CoOOH + 2e^- \quad (7)$$

$$CoOOH + OH \rightleftharpoons CoO_2 + H_2O + e^- \quad (8)$$

The observed anodic and cathodic peaks are in good agreement with previous reports.[13,32] With the increase of scan rate from 5 to 100 mV s^{-1}, the position of the cathodic peak slightly shifts from 0.28 to 0.24 V, indicating that the $NiCo_2O_4$ nanosheet electrode is favorable for fast redox reactions.[32,35] In contrast, the anodic peak is shifted to higher potential at higher scan rates; however the voltage window is not wide enough to show this shift. At low scan rates, the $NiCo_2O_4$ electrode can perform well as the ions from the KOH electrolyte have enough time to utilize both the outer and inner surface of the electrode. However, at higher scan rates, some irreversible redox reactions are observed as the area which can be occupied by the electrolyte ions decreases as a result of the decrease in diffusive path length.[36] The specific capacitances of the 2D $NiCo_2O_4$ nanosheets are 200, 198, 175, 150, 140, and 125 F g^{-1}, at scan rates of 5, 20, 40, 60, 80 and 100 mV s^{-1}, respectively, corresponding to a relatively high capacitance retention of 62.5%. In comparison, the specific capacitances of the $NiCo_2O_4$ nanospheres are 49.0, 23.0, 14.4, 10.2, 7.97, and 6.39 F g^{-1}, respectively, corresponding to a very low capacitance retention of 13% (Fig. 8c). These results clearly indicate the superiority of the 2D $NiCo_2O_4$ nanosheets in terms of both specific capacitance and capacitance retention, which may be attributed to their mesoporous features and much larger surface area which provide significantly more electroactive sites and improved diffusion of the electrolyte.[12] The explanations for the CV curves and specific capacitance *vs.* scan rate curves for the other metal cobaltite samples are provided in the notes for Fig. S7.†

A two-electrode asymmetric supercapacitor (ASC) cell was assembled using the porous 2D $NiCo_2O_4$ nanosheets as the positive electrode, GO as the negative electrode, and 3.0 M KOH aqueous solution as the electrolyte. The total weight loading on both electrodes was adjusted to 1 mg. As shown in Fig. 8d, by combining the $NiCo_2O_4$ cathode and GO anode, the cell voltage of the as-fabricated ASC can be expanded to 1.6 V without an obvious IR drop. Galvanostatic charge–discharge measurements were performed on the $NiCo_2O_4$ nanosheets//GO ASC cell and the discharge curves for current densities from 0.5 to 5 A g^{-1} are given in Fig. 8e. The specific capacitances of the ASC cell are 61.0, 58.7, 57.8, 55.2, 53.2, 49.8, 48.3 at current densities of 0.5, 0.7, 0.8, 1, 2, 3, 4, and 5 A g^{-1}, respectively, corresponding to a high capacitance retention of 75.8% (Fig. 8f). This value is better than previously reported ASCs based on Co_3O_4//AC (activated carbon) (46%),[37] $NiCo_2O_4$ nanosheets@HMRAs//AC

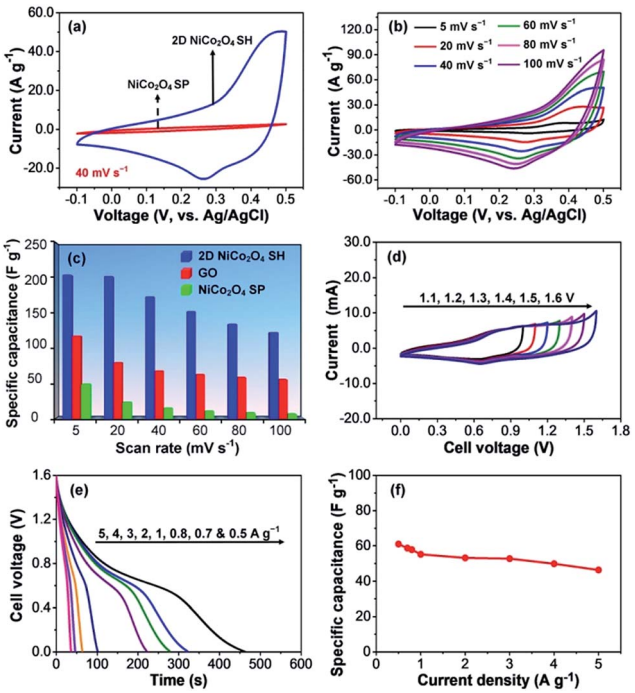

Fig. 8 (a) Comparison of CV curves between $NiCo_2O_4$ nanospheres and 2D $NiCo_2O_4$ nanosheets. (b) CV curves of 2D $NiCo_2O_4$ nanosheets at various scan rates from 5–100 mV s^{-1}. (c) Scan rate dependence of specific capacitance for $NiCo_2O_4$ nanospheres, 2D $NiCo_2O_4$ nanosheets, and GO. (d) Potential window variation for the upper potential windows ranging from 1.1 V to 1.5 V for ASC. (e) Galvanostatic discharge curves of the assembled 2D $NiCo_2O_4$ nanosheets//GO ASC at various current densities from 0.5 to 5 A g^{-1}. (f) Dependence of specific capacitance of the 2D $NiCo_2O_4$ nanosheets//GO ASC on the applied current density.

(46%),[38] $NiCo_2S_4$//AC (56%),[39] NC (nanoporous carbon)//NC (60%),[40] and $NiCo_2O_4$-NC//NC (56%).[41] The decrease in specific capacitance with the increase of current density can be correlated to the increased barrier to penetration and diffusion of electrolyte.[42] The good capacitance retention of the assembled $NiCo_2O_4$ nanosheets//GO ASC cell may be contributed by the small thickness (5–7 nm) and mesoporous feature of the as-synthesized 2D $NiCo_2O_4$ nanosheets and correspondingly their large surface area which can provide many electrochemically active sites for the redox reactions and facilitate the diffusion of the electrolyte, thereby leading to more efficient utilization of the active material.[12,32] Moreover, the well-interconnected nanosheets can facilitate better transport of the electrolyte, thus leading to improved capacitance retention.[14]

The Ragone plot (energy density *vs.* power density) of our ASC is given in Fig. S8b.† The assembled 2D $NiCo_2O_4$ NSs//GO ASC shows a high energy density of 38.53 W h kg^{-1} at a power density of 299.3 W kg^{-1} which decreases to 21.05 W h kg^{-1} at a higher power density of 340 W kg^{-1}. This energy density is higher than those of ASCs based on porous $NiCo_2O_4$//activated carbon (AC),[43] mesoporous $NiCo_2O_4$//AC,[44] $ZnCo_2O_4$ microspheres//AC,[45] $ZnCo_2O_4$ nanowires//AC,[46] $FeCo_2O_4$ nanowires//AC,[47] NiO nanopetals//AC,[48] and some hybrid materials, including $NiCo_2O_4$@-CQDs//AC,[49] $NiCo_2O_4$ NSs-CNTs//AC,[50] $NiCo_2O_4$-reduced graphene oxide (RGO)//AC,[34] Co_3O_4 NSs-RGO//AC,[51] and $NiCo_2O_4$–MnO_2//AG,[52] as summarized in Table S3.† The cycling performance of the ASC was evaluated by charge–discharge studies at a current density of 5 A g^{-1} up to 2000 cycles (Fig. S8c†). The assembled ASC cell exhibits good cycling stability with a high capacitance retention of 91% after 2000 cycles. This is better than previously reported ASCs based on porous $NiCo_2O_4$//AC (85% after 5000 cycles at 1.5 A g^{-1}),[43] $NiCo_2O_4$-RGO//AC (83% after 2500 cycles at 2 A g^{-1}),[34] $NiCo_2O_4$–MnO_2//AC (73.8% after 3000 cycles at 5 A g^{-1}),[52] Co_3O_4 nanosheets-RGO//AC (89% after 1000 cycles at 1 A g^{-1}),[51] and $ZnCo_2O_4$ microspheres//AC (76.68% after 1000 cycles at 0.5 A g^{-1}).[45] The SEM images of the $NiCo_2O_4$ nanosheet electrode after 2000 cycles at 5 A g^{-1} show that the sheet-like morphology is still well-maintained, albeit with some degree of agglomeration due to repeated charge–discharge processes (Fig. S9†). These results indicate the relatively good chemical stability of the fabricated $NiCo_2O_4$ nanosheets. In the future, the as-synthesized 2D metal cobaltite nanosheets can be hybridized with other metal oxides or carbon-based materials to improve their power density and specific capacitance further. However, in this work, we focus on showing the benefit of the proposed strategy for obtaining 2D metal cobaltite products with enhanced electrochemical performance.

4. Conclusions

In summary, we have developed a general template-free strategy for obtaining 2D mesoporous metal cobaltite nanosheets through the self-deconstruction/reconstruction of monodispersed Co-based metal glycerate nanospheres into 2D Co-based metal glycerate/hydroxide nanosheets followed by their calcination in air at a relatively low temperature of 260 °C. The self-deconstruction/reconstruction of the Co-based metal glycerate nanospheres is initiated by the released OH^- ions as a result of the "water treatment" process. The proposed general strategy is highly advantageous for generating 2D mixed oxide nanosheets with very high surface areas (150–200 m^2 g^{-1}) and mesoporous features with narrow pore size distribution at lower crystallization temperatures. Using the 2D mesoporous $NiCo_2O_4$ nanosheets synthesized *via* the proposed strategy as a representative sample, we found that they exhibit greater capacitance retention and much higher specific capacitance compared to the $NiCo_2O_4$ nanospheres achieved by the direct calcination of the Ni–Co glycerate nanospheres, thus highlighting the benefit of the proposed 'self-deconstruction/reconstruction' strategy for enhancing the electrochemical performance. Finally, the assembled 2D $NiCo_2O_4$ nanosheets//graphene oxide ASC shows a maximum energy density of 38.53 W h kg^{-1} and good cycling stability with a high capacitance retention of 91% after 2000 cycles at 5 A g^{-1}. It is expected that the proposed general strategy may be expanded to other transition metal elements for creating 2D mixed oxide nanosheets with greatly enhanced surface areas and functional performance.

Conflicts of interest

There are no conflicts to declare.

Acknowledgements

Y.V. Kaneti thanks the Japan Society for Promotion of Science (JSPS) providing the JSPS standard long-term postdoctoral fellowship. Y.V. Kaneti thanks Dr Jie Wang for the useful discussion regarding electrochemical performance. The authors acknowledge Namiki Foundry at NIMS for providing access to the characterization facilities used in this study. This work was supported by an Australian Research Council (ARC) Future Fellow FT150100479 and JSPS KAKENHI (Grant Numbers 17H05393 and 17K19044). This work was partly supported by the International Energy Joint R&D Program of the Korea Institute of Energy Technology Evaluation and Planning (KETEP), granted financial resource from the Ministry of Trade, Industry & Energy, Republic of Korea (No. 20168510011350).

References

1 H. Zhang, *ACS Nano*, 2015, **9**, 9451–9469.
2 L. Peng, P. Xiong, L. Ma, Y. Yuan, Y. Zhu, D. Chen, X. Luo, J. Lu, K. Amine and G. Yu, *Nat. Commun.*, 2017, **8**, 15139.
3 J. Bao, X. Zhang, B. Fan, J. Zhang, M. Zhou, W. Yang, X. Hu, H. Wang, B. Pan and Y. Xie, *Angew. Chem., Int. Ed.*, 2015, **54**, 7399–7404.
4 Y. V. Kaneti, J. Yue, X. Jiang and A. Yu, *J. Phys. Chem. C*, 2013, **117**, 13153–13162.
5 P. K. Kannan, D. J. Late, H. Morgan and C. S. Rout, *Nanoscale*, 2015, **7**, 13293–13312.
6 D. Deng, K. S. Novoselov, Q. Fu, N. Zheng, Z. Tian and X. Bao, *Nat. Nanotechnol.*, 2016, **11**, 218–230.
7 H. Cheng, T. Kamegawa, K. Mori and H. Yamashita, *Angew. Chem., Int. Ed.*, 2014, **53**, 2910–2914.
8 G. Fiori, F. Bonaccorso, G. Iannaccone, T. Palacios, D. Neumaier, A. Seabaugh, S. K. Banerjee and L. Colombo, *Nat. Nanotechnol.*, 2014, **9**, 768–779.
9 X. Xiao, H. Song, S. Lin, Y. Zhou, X. Zhan, Z. Hu, Q. Zhang, J. Sun, B. Yang, T. Li, L. Jiao, J. Zhou, J. Tang and Y. Gogotsi, *Nat. Commun.*, 2016, **7**, 11296.
10 Z. Sun, T. Liao, Y. Dou, S. M. Hwang, M.-S. Park, L. Jiang, J. H. Kim and S. X. Dou, *Nat. Commun.*, 2014, **5**, 3813.
11 Y. V. Kaneti, J. Tang, R. R. Salunkhe, X. Jiang, A. Yu, K. C. W. Wu and Y. Yamauchi, *Adv. Mater.*, 2017, **29**, 1604898.
12 G. Zhang and X. W. Lou, *Adv. Mater.*, 2013, **25**, 976–979.
13 T.-Y. Wei, C.-H. Chen, H.-C. Chien, S.-Y. Lu and C.-C. Hu, *Adv. Mater.*, 2010, **22**, 347–351.
14 J. Du, G. Zhou, H. Zhang, C. Cheng, J. Ma, W. Wei, L. Chen and T. Wang, *ACS Appl. Mater. Interfaces*, 2013, **5**, 7405–7409.
15 A. K. Mondal, D. Su, S. Chen, K. Kretschmer, X. Xie, H.-J. Ahn and G. Wang, *ChemPhysChem*, 2015, **16**, 169–175.
16 J. Liang, Z. Fan, S. Chen, S. Ding and G. Yang, *Chem. Mater.*, 2014, **26**, 4354–4360.
17 L.-Q. Mai, A. Minhas-Khan, X. Tian, K. M. Hercule, Y.-L. Zhao, X. Lin and X. Xu, *Nat. Commun.*, 2013, **4**, 2923.
18 P. Simon, Y. Gogotsi and B. Dunn, *Science*, 2014, **343**, 1210.
19 T. Brousse, D. Bélanger and J. W. Long, *J. Electrochem. Soc.*, 2015, **162**, A5185–A5189.
20 F.-X. Ma, H. Hu, H. B. Wu, C.-Y. Xu, Z. Xu, L. Zhen and X. W. Lou, *Adv. Mater.*, 2015, **27**, 4097–4101.
21 Y. Wang, L. Yu and X. W. Lou, *Angew. Chem., Int. Ed.*, 2016, **55**, 7423–7426.
22 L. Shen, L. Yu, X.-Y. Yu, X. Zhang and X. W. Lou, *Angew. Chem., Int. Ed.*, 2015, **54**, 1868–1872.
23 Y. Yang, S. Wang, C. Jiang, Q. Lu, Z. Tang and X. Wang, *Chem. Mater.*, 2016, **28**, 2417–2423.
24 C. Xing, F. Musharavati, H. Li, E. Zalezhad, O. K. S. Hui, S. Bae and B.-Y. Cho, *RSC Adv.*, 2017, **7**, 38945–38950.
25 J. Zhao, Y. Zou, X. Zou, T. Bai, Y. Liu, R. Gao, D. Wang and G.-D. Li, *Nanoscale*, 2014, **6**, 7255–7262.
26 D. Larcher, G. Sudant, R. Patrice and J. M. Tarascon, *Chem. Mater.*, 2003, **15**, 3543–3551.
27 X. Yu, Z. Sun, Z. Yan, B. Xiang, X. Liu and P. Du, *J. Mater. Chem. A*, 2014, **2**, 20823–20831.
28 R. Chen, H.-Y. Wang, J. Miao, H. Yang and B. Liu, *Nano Energy*, 2015, **11**, 333–340.
29 S. G. Mohamed, Y.-Q. Tsai, C.-J. Chen, Y.-T. Tsai, T.-F. Hung, W.-S. Chang and R.-S. Liu, *ACS Appl. Mater. Interfaces*, 2015, **7**, 12038–12046.
30 W. Luo, X. Hu, Y. Sun and Y. Huang, *J. Mater. Chem.*, 2012, **22**, 8916–8921.
31 W. Guo, Y. E, L. Gao, L. Fan and S. Yang, *Chem. Commun.*, 2010, **46**, 1290–1292.
32 Y. Chen, B. Qu, L. Hu, Z. Xu, Q. Li and T. Wang, *Nanoscale*, 2013, **5**, 9812–9820.
33 S. Khalid, C. Cao, L. Wang and Y. Zhu, *Sci. Rep.*, 2016, **6**, 22699.
34 X. Wang, W. S. Liu, X. Lu and P. S. Lee, *J. Mater. Chem.*, 2012, **22**, 23114–23119.
35 C. Yuan, J. Li, L. Hou, X. Zhang, L. Shen and X. W. Lou, *Adv. Funct. Mater.*, 2012, **22**, 4592–4597.
36 S. S. Rao, I. K. Durga, N. Kundakarla, D. Punnoose, C. V. V. M. Gopi, A. E. Reddy, M. Jagadeesh and H.-J. Kim, *New J. Chem.*, 2017, **41**, 10037–10047.
37 X. Wang, M. Li, Z. Chang, Y. Wang, B. Chen, L. Zhang and Y. Wu, *J. Electrochem. Soc.*, 2015, **162**, A1966–A1971.
38 X.-F. Lu, D.-J. Wu, R.-Z. Li, Q. Li, S.-H. Ye, Y.-X. Tong and G.-R. Li, *J. Mater. Chem. A*, 2014, **2**, 4706–4713.
39 Z. Wu, X. Pu, X. Ji, Y. Zhu, M. Jing, Q. Chen and F. Jiao, *Electrochim. Acta*, 2015, **174**, 238–245.
40 C. Young, R. R. Salunkhe, J. Tang, C.-C. Hu, M. Shahabuddin, E. Yanmaz, M. S. A. Hossain, J. H. Kim and Y. Yamauchi, *Phys. Chem. Chem. Phys.*, 2016, **18**, 29308–29315.
41 C. Young, R. R. Salunkhe, S. M. Alshehri, T. Ahamad, Z. Huang, J. Henzie and Y. Yamauchi, *J. Mater. Chem. A*, 2017, **5**, 11834–11839.
42 R. R. Salunkhe, J. Lin, V. Malgras, S. X. Dou, J. H. Kim and Y. Yamauchi, *Nano Energy*, 2015, **11**, 211–218.
43 R. Ding, L. Qi, M. Jia and H. Wang, *Electrochim. Acta*, 2013, **107**, 494–502.
44 M. J. Pang, S. Jiang, G. H. Long, Y. Ji, W. Han, B. Wang, X. L. Liu, Y. L. Xi, F. Z. Xu and G. D. Wei, *RSC Adv.*, 2016, **6**, 67839–67848.

45 Y. Gai, Y. Shang, L. Gong, L. Su, L. Hao, F. Dong and J. Li, *RSC Adv.*, 2017, **7**, 1038–1044.
46 C. Wu, J. Cai, Q. Zhang, X. Zhou, Y. Zhu, P. K. Shen and K. Zhang, *ACS Appl. Mater. Interfaces*, 2015, **7**, 26512–26521.
47 A. Pendashteh, J. Palma, M. Anderson and R. Marcilla, *J. Mater. Chem. A*, 2015, **3**, 16849–16859.
48 G. Cheng, Q. Bai, C. Si, W. Yang, C. Dong, H. Wang, Y. Gao and Z. Zhang, *RSC Adv.*, 2015, **5**, 15042–15051.
49 Y. Zhu, Z. Wu, M. Jing, H. Hou, Y. Yang, Y. Zhang, X. Yang, W. Song, X. Jia and X. Ji, *J. Mater. Chem. A*, 2015, **3**, 866–877.
50 F. Cai, Y. Kang, H. Chen, M. Chen and Q. Li, *J. Mater. Chem. A*, 2014, **2**, 11509–11515.
51 C. Yuan, L. Zhang, L. Hou, G. Pang and W.-C. Oh, *RSC Adv.*, 2014, **4**, 14408–14413.
52 M. Kuang, Z. Q. Wen, X. L. Guo, S. M. Zhang and Y. X. Zhang, *J. Power Sources*, 2014, **270**, 426–433.